crystals

MDPI

Article

Encapsulated Passivation of Perovskite Quantum Dot ($CsPbBr_3$) Using a Hot-Melt Adhesive (EVA-TPR) for Enhanced Optical Stability and Efficiency

Saradh Prasad [1,2], Mamduh J. Aljaafreh [1], Mohamad S. AlSalhi [1,2,*] and Abeer Alshammari [1]

[1] Department of Physics and Astronomy, College of Science, King Saud University, 11451 Riyadh, Saudi Arabia; srajendra@ksu.edu.sa (S.P.); maljaafreh@ksu.edu.sa (M.J.A.); Aalshammri@ksu.edu.sa (A.A.)
[2] Research Chair on Laser Diagnosis of Cancers, Department of Physics and Astronomy, College of Science, King Saud University, 11451 Riyadh, Saudi Arabia
* Correspondence: malsalhi@ksu.edu.sa; Tel.: +966-50-510-4815

Abstract: The notable photophysical characteristics of perovskite quantum dots (PQDs) ($CsPbBr_3$) are suitable for optoelectronic devices. However, the performance of PQDs is unstable because of their surface defects. One way to address the instability is to passivate PQDs using different organic (polymers, oligomers, and dendrimers) or inorganic (ZnS, PbS) materials. In this study, we performed steady-state spectroscopic investigations to measure the photoluminescence (PL), absorption (A), transmission (T), and reflectance (R) of perovskite quantum dots ($CsPbBr_3$) and ethylene vinyl acetate/terpene phenol (1%) (EVA-TPR (1%), or EVA) copolymer/perovskite composites in thin films with a thickness of 352 ± 5 nm. EVA is highly transparent because of its large band gap; furthermore, it is inexpensive and easy to process. However, the compatibility between PQDs and EVA should be established; therefore, a series of analyses was performed to compute parameters, such as the band gap, the coefficients of absorbance and extinction, the index of refractivity, and the dielectric constant (real and imaginary parts), from the data obtained from the above investigation. Finally, the optical conductivities of the films were studied. All these analyses showed that the EVA/PQDs were more efficient and stable both physically and optically. Hence, EVA/PQDs could become copolymer/perovskite active materials suitable for optoelectronic devices, such as solar cells and perovskite/polymer light-emitting diodes (PPLEDs).

Keywords: perovskite quantum dots; hot-melt adhesive; ethylene-vinyl acetate (EVA); terpene-phenol (TPR); thin films

check for updates

Citation: Prasad, S.; Aljaafreh, M.J.; AlSalhi, M.S.; Alshammari, A. Encapsulated Passivation of Perovskite Quantum Dot ($CsPbBr_3$) Using a Hot-Melt Adhesive (EVA-TPR) for Enhanced Optical Stability and Efficiency. *Crystals* **2021**, *11*, 419. https://doi.org/10.3390/cryst11040419

Academic Editors: Assem Barakat and Alexander S. Novikov

Received: 25 March 2021
Accepted: 11 April 2021
Published: 13 April 2021

Publisher's Note: MDPI stays neutral with regard to jurisdictional claims in published maps and institutional affiliations.

Copyright: © 2021 by the authors. Licensee MDPI, Basel, Switzerland. This article is an open access article distributed under the terms and conditions of the Creative Commons Attribution (CC BY) license (https://creativecommons.org/licenses/by/4.0/).

1. Introduction

Perovskite was discovered in 1873 and has a basic structure of ABX_3, where A and B are cations and X is an anion. The cations can adopt three types of pairing ratios: 2:4 perovskites $\left(A^{2+}B^{4+}\left(X^{-2}\right)_3\right)$, 3:3 perovskites $\left(\left(A^{3+}B^{3+}\left(X^{-2}\right)_3\right)\right.$, and 1:5 perovskites $\left[/\left(A^{+}B^{5+}\left(X^{-2}\right)_3\right)\right.$. The structure of perovskite has been known since 1945. However, a major breakthrough did not come until the foremost efficient solid-state perovskite solar cell was disclosed in 2012 [1]. In the last decade, perovskites have become a common name in laboratories because of the advent of organic, organic–inorganic, and inorganic perovskites [2–5]. In particular, organometal and inorganic perovskites have been found to be very efficient sensors, X-ray imaging materials [6], lasers [7], and light-emitting and photovoltaic devices because of their long-range charge carrier diffusion lengths [8–10], high photoluminescence (PL), quantum yield (QY), and high absorption coefficients [11]. Organohalide perovskites were found to be an efficient solar material. The bands of organohalide perovskites can be tuned using different organic and halide compositions [12], which is useful for designing a broad range of devices. The chemical stability of organohalides was found to be lower [13].

Organic–inorganic (hybrid halides) and inorganic lead can be synthesized as bulk microcrystalline and nanocrystalline structures, such as perovskite quantum dots. Perovskite quantum dots show very good stability compared with other perovskite materials. Quantum dot-based perovskites have the advantages of wavelength tunability, a highly controllable synthesis, and an easy solution processability. Organometal halide perovskite quantum dots have been synthesized by various research teams [14,15]. Similarly, inorganic halide perovskite quantum dots with very high efficiency were synthesized by Protesescu et al. in 2015 [16]. Despite their remarkable optoelectronic properties, perovskite-based quantum dots have issues such as susceptibility to moisture due to their hygroscopic nature and their anion-exchange reactions. Moreover, they are very unstable under thermal heating or vigorous agitation (sonication). The crystal lattice formation energy is inherently low, and the migration of surface ions poses an extreme challenge to their stability.

Consequently, it is necessary to find an effective technique for enhancing the stability. Numerous protective strategies, including surface passivation, in situ shell layer development, and treatment with erosive species to generate an altered perovskite layer with low activity that insulates perovskite quantum dots (PQDs) from vulnerability and protects or even improves the desired properties [17–21], have been advocated to enhance the stability of PQDs.

Notably, a single-step synthesis using the doping agent $Co(AC)_2$ on a $CsPbBr_3$ QD surface improved the photoluminescence quantum yield (PLQY) by up to 90%, and it was maintained at over 65% for nearly two months [22]. Atomic layer deposition (ALD) was utilized to synthesize core-shell-like QD-silica luminescent spheres ($CsPbBr_3$ QD-SLSs). The synthesis took advantage of the intrinsic reactivity differences toward the precursors; hence, the defect sites on the surface of the $CsPbBr_3$ QDs were specifically passivated [23]. Ye Wu et al. proposed an in situ $PbBr_6^{4-}$ octahedra passivation approach for nanoplates and quantum dots of blue-emitting $CsPbBr_3$, achieving an absolute QY of 96% [24]. The utility of organic, organometallic, and inorganic passivation has been demonstrated by many groups [25–27].

Small molecules, oligomers, and polymers can be used to protect perovskite quantum ($CsPbBr_3$) dots. These molecules can facilitate energy transfer in addition to offering protection. A series of theoretically significant polymer materials, such as poly(methyl methacrylate) (PMMA), polycarbonate (PC), polystyrene (PS), polyvinyl chloride (PVC), cellulose acetate (CA), and acrylonitrile butadiene styrene (ABS), were swollen in a dimethylformamide (DMF) environment, infused with PQDs, and finally shrunk to fabricate solid-state substrates using the solvent DMF to illustrate the generality of this strategy [20]. A perovskite–polymer composite was made using ligand-assisted swelling-deswelling microencapsulation to enhance the stability of the perovskite [28]. Extremely luminescent colloidal PQDs made of $MAPbX_3$ and $CsPbX_3$ ($MA = CH_3NH_3^+$, X = Cl, Br, I) were passivated using polyvinylidene fluoride (PVDF). The hydrophobic semi-crystalline polymer polyvinylidene fluoride (PVDF) was used as a host for highly luminescent colloidal $MAPbX_3$ and $CsPbX_3$ ($MA = CH3NH^{3+}$, X = Cl, Br, I) quantum dots (QDs), and the stability was improved dramatically. L. C. Chen et al analyzed the influence of PMMA on PQDs. They used a sophisticated system to fabricate PMMA/PQDs [29]. Lead halide perovskite nanocrystals were blended with the polymer poly(isobutylene-alt-maleic anhydride)-graft-dodecyl (PMA) and found to be stable for a prolonged period [30]. Flexible LEDs were fabricated by encapsulating perovskite inside poly(ethylene oxide)-modified poly(3,4-ethylenedioxythiophene) polystyrene sulfonate. The LED was flexible and mechanically robust for up to 100 cycles at 40% strain. The in situ encapsulation of perovskites was achieved by combining EVA and the perovskite precursor ($PbBr_2$ and CsBr) in toluene, and, upon supersaturation, three PQD/EVA films were formed [31].

In this report, we describe a post-synthesis encapsulation technique for green-emitting $CsPbBr_3$ quantum dots using simple solvent dispersion and exploitation of the glass transition by mild heating. This method is not limited to thin films but can be used to form solid-state perovskite-embedded matrices of any size and shape. However, it also results

in thin films of ethylene vinyl acetate/terpene phenol (EVA-TPR) both as separate layers (glass/PQDs/EVA-TPR) and as composites (glass/PQDs:EVA-TPR). To the best of our knowledge, this is the first study on PQD/EVA-TPR encapsulation.

2. Materials and Methods

Figure 1a–c illustrates the chemical structure of terpene phenol (TPR), the structure of ethylene vinyl acetate (EVA), and the $CsPbBr_3$ crystal structure, respectively. The host material was a commercially and readily available EVA-TRP glue stick selected because of its excellent transparency. The LUMAR PQDs were obtained from Quantum Solutions, Tuwal, Saudi Arabia.

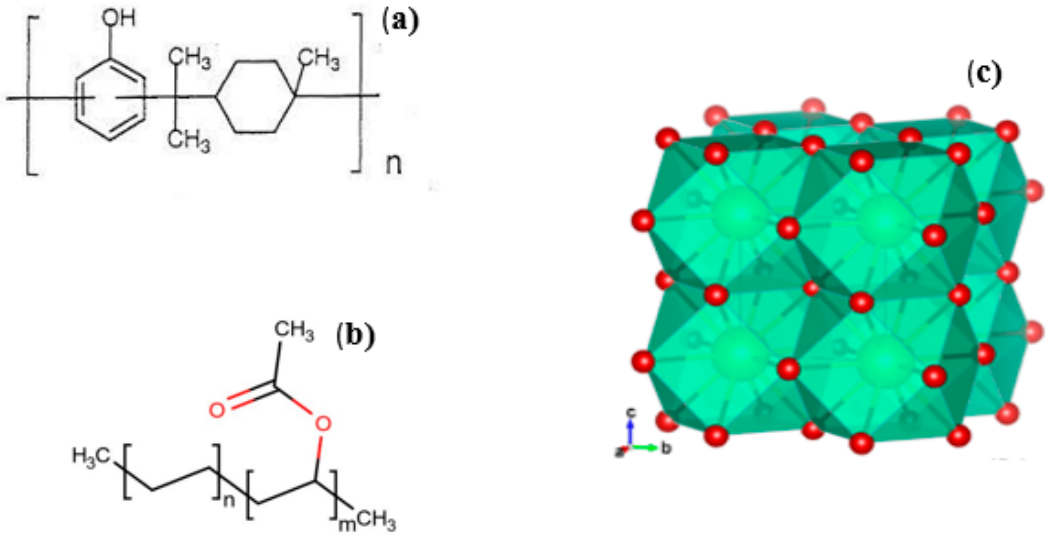

Figure 1. The molecular structures of (**a**) terpene phenol (TPR) and (**b**) ethylene vinyl acetate (EVA) obtained using the MarvinSketch 20.4 software and (**c**) the crystal structure of a unit of cesium lead tribromide ($CsPbBr_3$) drawn with the VESTA software.

A spectrofluorometer (LS 55, from Perkin Elmer, Llantrisant, United Kingdom) was employed to evaluate the photoluminescence (PL) spectra, and a Perkin Elmer Lambda 950 spectrophotometer (Llantrisant, United Kingdom) was utilized to investigate the absorption spectra of the film samples in the range of 100 to 1100 nm. The spectral dependencies of the transmittance and reflectance of the film were obtained using a UV-vis near-infrared spectrophotometer (Cary 5000, Varian, Australia). Transmission electron microscopy (TEM) characterization of the PQDs and PQDs: EVA-TPR films was accomplished using a JEM-1011 instrument (JEOL, Tokyo, Japan) at an accelerating voltage of 200 kV. The structural properties of the films were characterized by an X-ray diffraction system using a copper (Cu) target (λ = 1.54060 Å, 2θ = 10°–50°, Miniflex 600, Rigaku, Japan).

All solvents are procured from Sigma Aldrich, St. Louis, MO, USA. The substrates were cleaned with a non-ionic surfactant liquid, acetone, ethanol, and deionized (DI) water at least 3 times for 5 min each cycle. Next, the $CsPbBr_3$ QDs were dissolved in toluene to obtain a concentration of 20 mg/mL. Similarly, EVA-TRP was dissolved in toluene to a concentration of 50 mg/mL. To homogenize the solution, it was heated and stirred constantly for 10 min and then allowed to cool to room temperature. The two solutions were mixed at a ratio of 1:1 to form the final composite (EVA-TRP/PQD) solution. For spin coating, the cleaned substrate was loaded on a spin coater holder (KW-4A Spin Coater, Chemat Technology, Inc., Northridge, CA, USA), and 75 µL of the EVA-TRP/PQDs were dropped onto the substrate, which was spun at a low speed for 5 s and at 2000 rpm for 20 s to create a highly uniform thin film. The film was annealed at 80°C for 3 min and then vacuum-dried for 30 min to give a thin film. The thickness of the films was assessed using a Dektak XT stylus profilometer (Billerica, MA, USA).

3. Results and Discussion

3.1. Structural Characteristics of the Pure PQDs and the EVA-TPR/PQD Composite

Figure 2a,b presents the structural (TEM) characteristics of the pure PQDs and the EVA-TPR/PQD composite. The average sizes of the pure PQDs and the EVA-TPR/PQD composite were 11.3 nm and 9.3 nm, respectively. The size of the composite was smaller than that of the pure PQDs because of the compression force exerted by the EVA-TRP copolymer; additionally, mild sonication was used, which damaged a few scattered PQDs, as shown in Figure 2a,b. Figure 2a shows closely compacted, well-arranged PQDs, whereas Figure 2b shows that the addition of EVA-TPR increased the distortion, and the spacing between adjacent PQDs also increased. Furthermore, the TEM images also showed that the interplanar distance corresponding to adjacent cesium atoms was 0.52 nm. Figure 2b shows the presence of EVA-TPR at the boundary of ligands.

The XRD patterns shown in Figure 2c also corroborate the TEM analysis. The calculated results for the pure PQDs and EVA-TPR/PQD composite were 9.7 nm and 7.89 nm, respectively. The XRD patterns exhibited peaks at 2θ = 15.33°, 21.70°, 30.87°, 34.45°, 37.90°, and 43.93° correlated to diffractions from the (100), (110), (200), (210), (211), and (220) planes of the pure PQDs and EVA-TPR/PQDs. The peaks did not shift but appeared to broaden (full-width half-maximum) owing to the adherence between EVA-TPR and the PQDs. The XRD patterns of both samples had similar features, and the XRD patterns of the sample with the EVA-TPR/PQD surface did not exhibit an additional peak because the pure EVA peak at 15.8° coincided with the PQD peak, and polymers tend to be amorphous, resulting in the broadening of the band at this peak location. All these observations from the experimental analysis show that the addition of EVA does not interfere with or result in detrimental changes to the PQDs, and EVA has good compatibility with them. The diameter of the crystallite size (D), the dislocation density (δ), and the microstrain (ε) in the film can be assessed using the XRD results and the following formulas:

$$D = \frac{K\lambda}{\beta \cdot cos\theta}, \ \delta = \frac{1}{D^2}, \text{ and } \varepsilon = \frac{\beta \cdot cos\theta}{4} \quad (1)$$

where k, which corresponds to the shape factor, has a typical value of approximately 0.9; the wavelength of the incident X-ray source λ is 0.154 nm; β is the full-width at half-maximum (FWHM) in radians; and θ is Bragg's angle. The dislocation density (δ) and the number of crystallites per unit area (N) were estimated using Equation (1) [32–34]. It was observed that the $CsPbBr_3$-PQD film had a grain size of 9.7 nm, which was consistent with the measurements attained from the TEM analysis (Figure 2a). Table 1 consolidates the structural factors for all samples.

Table 1. Structure of the EVA-modified PQD and the pure PQD thin films in the (110) plane.

PQDs	Full-Width Half-Maximum (deg)	D (nm)	Lattice Strain € × 10^{-3}	Dislocation Density × 10^{-2} $(nm)^{-2}$
EVA	3.16	2.55	13.59	15.38
PQD	0.83	9.70	3.57	1.061
EVA/PQD	1.02	7.89	4.39	1.604

3.2. Optical Properties of the Pure PQDs and the EVA-TPR/PQD Composite

Optical properties are a manifestation of the electronic transitions and the band gap of a nanomaterial. Fundamental optical properties such as absorption, photoluminescence, reflectivity, transmission, and refraction provide insights into the band structure, the electron-hole excitation, and the recombination efficiency. To compare the optical performances of the pure PQDs and the EVA-TPR/PQDs, the above experiments were performed for both samples. The photoluminescences (PL) of the pure PQDs and EVA-TPR/PQDs are

shown in Figure 3, with film thicknesses of 305 nm and 352 nm, respectively. The peak emissions of the pure PQDs and EVA-TPR/PQDs occurred at 522 nm and 520 nm, respectively, with FWHMs of 17 nm and 21 nm, respectively. The PL intensity of the EVA-TPR/PQDs was twice that of the PQDs at the same spin speed. The reason for this improvement could be fully understood by studying the absorption, transmission and reflectance, which enables a clear reason for the improved optical properties to be determined.

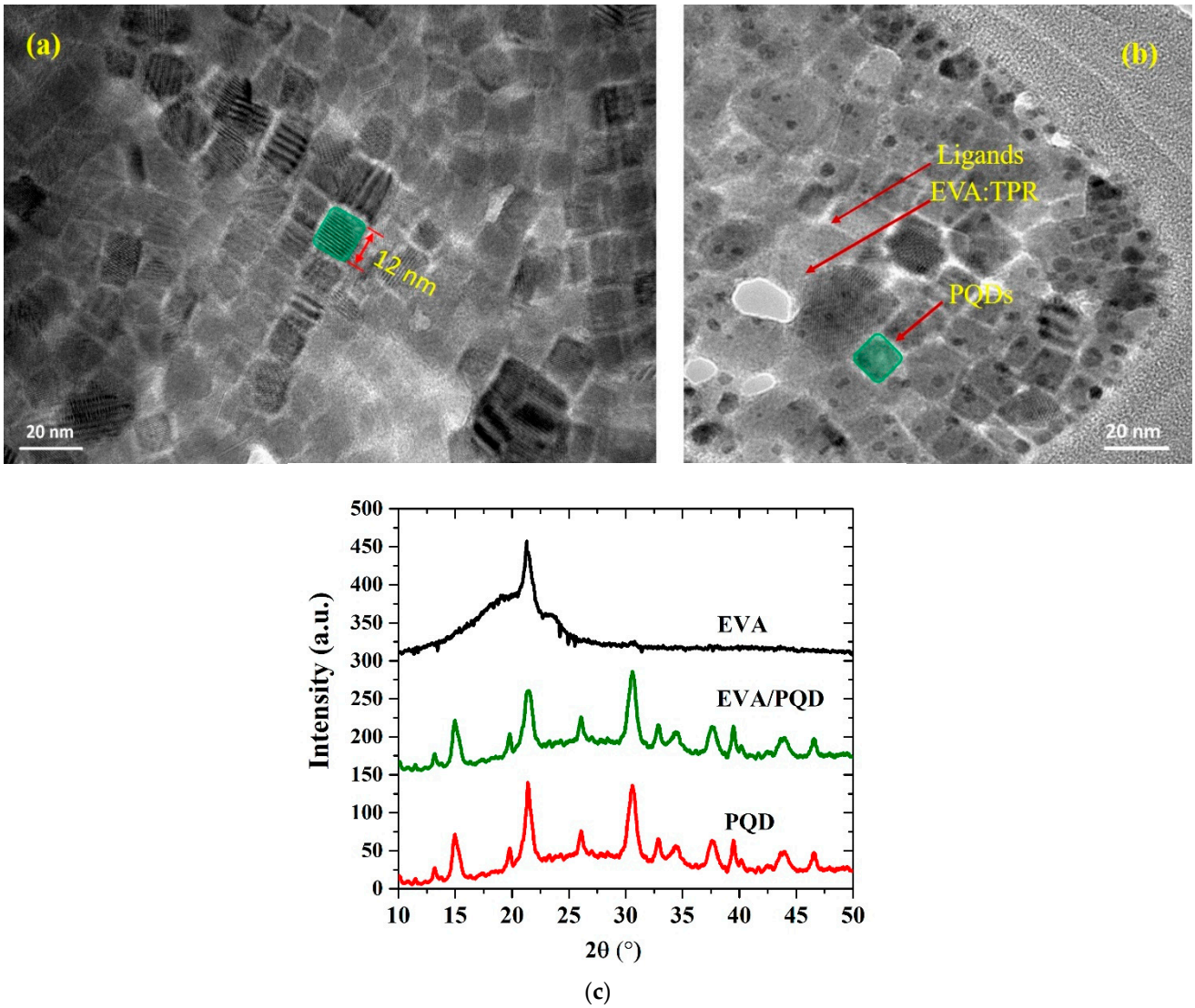

Figure 2. TEM images of (**a**) pure perovskite quantum dots (PQDs) and (**b**) PQDs: ethylene vinyl acetate/terpene phenol (EVA-TPR) at a scale of 20 nm. (**c**) XRD patterns of the pure EVA, the pure PQDs, and the PQD: EVA-TPR films.

Figure 4a shows that both samples (the PQD and the EVA/PQD films) have a broad optical absorption profile, with a primary shoulder band at 506 ± 1 nm, and the absorbance continuously upsurges with decreasing wavelength in the shorter wavelength region before the shoulder (500–350 nm). This trend is typical of QDs because of their quasi-continuous higher-order band gaps in the conduction band. In the case of the EVA-TPR/PQDs, the primary shoulder band appeared at 507 nm, and the absorption profile was similar to that of the pure PQDs. However, a tail was observed after the primary shoulder, which could be the result of the amorphous nature of the EVA-TPR polymer, but its absorbance was higher than that of the pure PQDs, which was attributed to the higher transparency, higher reflectivity, and smoother surface (glass transition) of the EVA-TPR polymer. The

absorption improvements at the band edge are due to resonant exciton creation, which plausibly explains the primarily steep rise in the absorption coefficient [16].

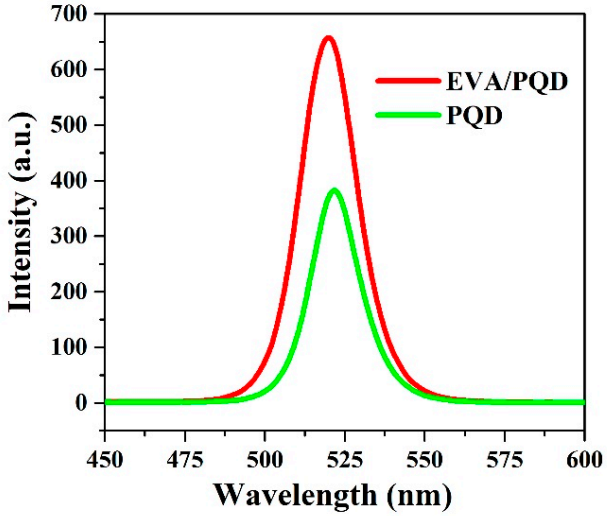

Figure 3. PL spectra of the EVA-TPR/ PQD surface and the pure PQD thin films. The excitation wavelength was 355 nm.

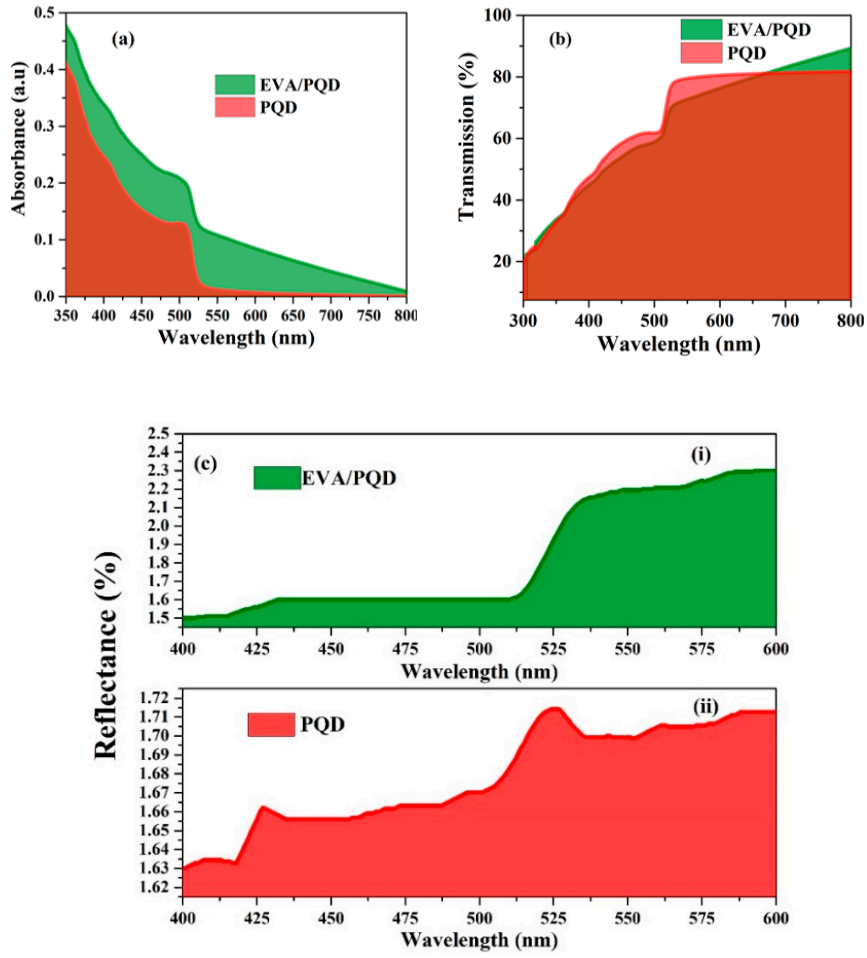

Figure 4. (**a**–**c**) Comparison of the absorbances, transmittances, and reflectances of the pure PQD and the EVA-TPR/PQD films.

Figure 4b illustrate the transmittance (T) of pure PQDs and EVA-TPR/PQD films with thicknesses of 305 nm and 352 nm, respectively. At shorter wavelengths, the transmittance increased linearly up to the transparency transition point at 510 nm; specifically, it increased from 20% at 300 nm to approximately 55% at 510 nm. At 510 nm, the transmittance rose sharply from 62% to 79%, which indicates a band gap transition corresponding to a band gap value of 2.43 eV. However, this information does not provide details about whether the band gap is direct or indirect, which was further investigated in this study. For the composite, a similar trend was observed, with the transition occurring from 59% to 71%. The transmittance changed distinctively and linearly with increasing transmission from 75% to 85% at wavelengths longer than 525 nm, which could be due to the amorphous nature of EVA.

Figure 4c(i) illustrates the experimentally measured reflectance spectra (R) of the pure PQD and the EVA-TPR/PQD films with thicknesses of 305 nm and 352 nm, respectively. The spectral profile of the reflectance of the pure PQDs exhibited a peak at 522 nm, and the reflectance increased linearly from 350 nm to 600 nm and beyond. The spectral profile of the pure PQDs was wavy and had two peaks at 426 nm and 522 nm, which corresponded to the reflectance originating from the discontinuity in the conduction band and the PQDs, respectively. The variations in the pure PQDs could be attributed to surface roughness-induced scattering. Figure 4c (ii) demonstrates the experimentally measured reflectance (R) spectrum of the EVA-TPR/PQD films. The EVA-TPR/PQDs generated a reflectance spectral profile with very smooth features and a clear surge in the transition band. Two plateaus were observed before and after the transition band. The spectral profile of the EVA-TPR/PQDs had two shoulders at 430 nm and 530 nm corresponding to the reflectance originating from the ligands and the PQDs, respectively. EVA did not interfere with the reflectance profile, indicating that EVA smoothed the surface, reducing the roughness and thus the scattering.

Next, the Tauc relationship was used to obtain the band gap information by identifying the fundamental absorption edge as follows:

$$(\alpha h\nu)^n = B_S\,(h\upsilon - E_g) \tag{2}$$

where B_S is a constant, E_g is the band gap, and the values of n are 2 and 1/2 for direct and indirect transitions, respectively [35,36]. The complete profiles of the direct and indirect band gaps as a function of energy (vis-a-vis wavelength) could be obtained from a Tauc analysis using the optical absorbance information from Equation (2). Plotting $(\alpha h\nu)^n$ versus $h\nu$ is a direct method for defining the nature of the optical transition. The natures of the direct and indirect allowed transitions can be compared using n = 2 and n = $\frac{1}{2}$, respectively, and n = 3 and n = 3/2 can be used to compare indirect and direct forbidden transitions, respectively [37]. The direct and indirect allowed transitions are explored in Figure 5. Figure 5a compares the direct band gap of the pure PQDs with that of the EVA-TPR/PQDs. The intersection of the transition slopes at $\alpha = 0$ gave a band gap of 2.33 eV for the latter, and the former had an energy gap of 2.38 eV (difference = 0.05 eV). Similar behavior was observed in the indirect band gap calculations for the pure and composite PQDs; the calculated band gaps were 2.202 eV and 2.304 eV, respectively, as depicted in Figure 5b. We can infer that the plot of $(\alpha h\nu)^2$ vs $h\nu$ has a steeper slope near the absorption edge of the optical spectra than the $(\alpha h\nu)^{1/2}$ vs $h\nu$ plot; moreover, there is a high degree of proximity between the allowed direct and indirect transitions, resulting in an improved direct resonant excitonic transition and thus improved photoluminescence efficiency. We can deduce that the direct band gap of the composite PQDs was steeper than that of the pure PQDs because of the improved surface emission and quantum efficiency.

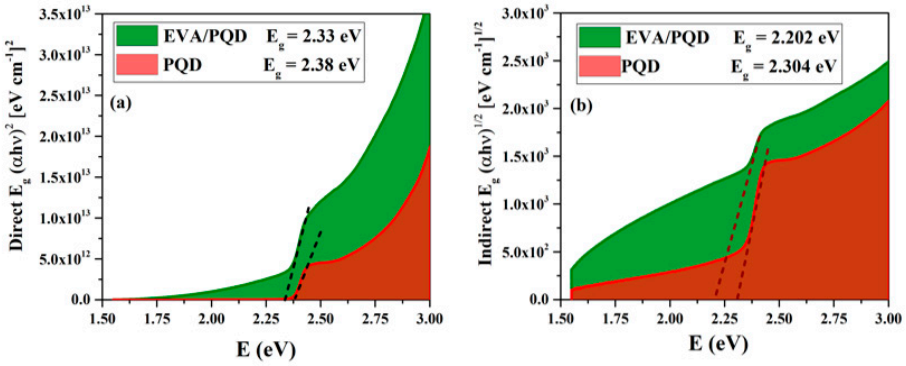

Figure 5. (**a**) Direct and (**b**) indirect band gaps of the pure PQD and the EVA-TPR/PQD films.

The profiles of the absorption coefficients of both films are shown as a function of wavelength in Figure 6 and were calculated using $\left(\alpha = \frac{2.303xA}{l}\right)$ [38–40], where A is the absorbance and l is the thickness of the film. The features of α(λ) are closely related to the absorbance spectra. At longer wavelengths (510 nm), α(λ) is very low for the pure film and increases linearly for the composite film. Then, α(λ) surges sharply from 0.21 to 1 for the pure film and less sharply from 0.76 to 1.2 for the composite film at 508 ± 2 nm. This indicates that the optical properties of the PQD composite were improved. The high absorption coefficient values and inherently protective passivation by EVA clearly demonstrate that EVA is capable of being an active layer in solar cell optoelectronic devices. The high α(λ) is evidence of high excitonic creation in the excited states, and the excitons have the potential for high conversion to charge carriers, which is crucial for the effective light harvesting of the materials [35,41,42].

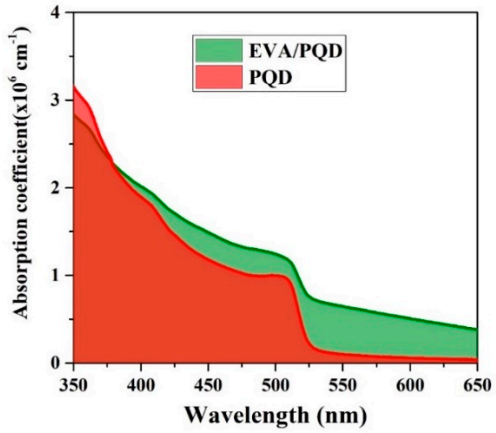

Figure 6. Absorption coefficients of the pure PQD and the EVA-TPR/PQD films.

The complex refractive index (N = n + ik) is a function of two parts, real and imaginary, where n is the real part of the refractive index and k is the imaginary part. The k value can be determined from experimentally measured parameters such as α(λ) using the equation $k = \alpha\lambda/4\pi$, and the n(λ) value can be calculated in terms of R using $n = (1+\sqrt{R})/(1-\sqrt{R})$ for the perpendicular incidence of light with respect to the film plane [43]. The wavelength-dependent functions k(λ) and n(λ) are presented in Figure 7a,b, respectively, for the pure and composite thin films. The profiles were identical to those of the absorption coefficient, with a shoulder at 506 ± 2 nm (508 nm for pure and 504 nm for composite), and k(λ) increased with increasing photon energy (decreasing wavelength). The value of k(λ) at the shoulder was approximately 0.039 and 0.049 for the pure and composite PQDs, respectively, which shows that the extinction efficiency of the EVA-TPR/PQDs was 25.6% higher than that of the pure PQDs; hence, EVA-TPR/PQDs are an attractive option for optoelectronic devices such as solar cells. Moreover, if proper pumping is applied, it could also serve as

a laser material. The electric field (EF) of the incoming photons interacting with the EF of a medium results in a slowing down of the photons. This phenomenon depends on the energy of the photon and is thus inversely dependent on the wavelength and is called the refractive index. The refractive index is an important parameter for identifying the efficiency of the medium and is used in all geometric optical designs of optical devices. The calculated refractive index n(λ) of the pure PQDs exhibited a distinct peak at 506 nm with a value of 1.70 and a range from 1.67 to 1.71, indicating that a large amount of light will not enter the medium and that pure PQDs would result in low-efficiency devices (e.g., solar cells and PQLEDs). On the other hand, the PQDs embedded in the EVA-TPR copolymer films had a reduced refractive index with a value of approximately 1.29 ± 0.01 at shorter wavelengths of up to 508 nm (transition region) and 1.34 ± 0.01 at longer wavelengths, and the features were smooth; therefore, the photons enter at a more oblique angle, making this material suitable for light-harvesting devices.

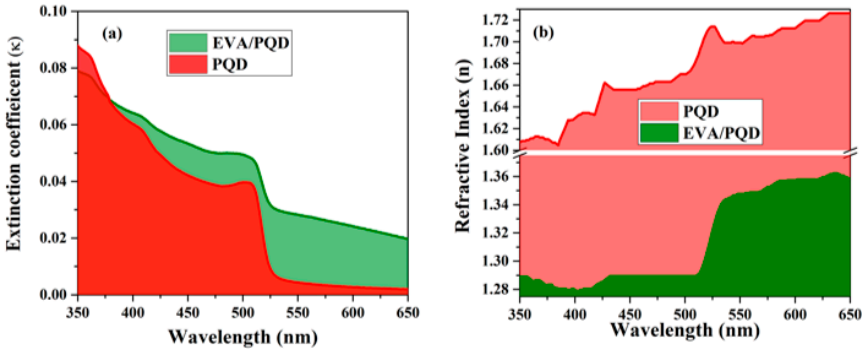

Figure 7. Computed (**a**) extinction coefficients k(λ) and (**b**) refractive indices n(λ) of the pure PQD and the EVA-TPR/PQD films.

The polarizability of a medium is a function of its dielectric constant. For all optoelectronic devices, the relative permittivity is an important factor that determines the performance, and it is a complex value composed of real (ε_r) and imaginary (ε_i) relative permittivities, as given in Equation (3) below [44].

$$\varepsilon = \varepsilon_r + \epsilon_i \quad (3)$$

$$\epsilon_r = n^2 - k^2$$

$$\epsilon_i = 2nk$$

The real part of the relative permittivity is plotted vs the wavelength (nm) in Figure 8a,b. At shorter wavelengths, that is, in the 350–650 nm region, ε_r was high. However, for the composite, the value was similarly lower at shorter wavelengths of up to 506 nm and increased at longer wavelengths. The imaginary part of the dielectric constant is given in Figure 8b. Its profile is similar to the absorption spectra with transitions at 508 and 506 nm for the pure PQDs and the composite. This result indicates that the composite PQD films are suitable for device fabrication, especially for optically and electrically pumped devices.

The calculated optical conductivity is perhaps the most important indicator for determining the feasibility of employing a film in devices such as PQLEDs, solar cells, and optoelectronic devices. The photoconductivity is important because it reveals information about the optical carrier generation, transport, and recombination processes within a device. The optical conductivities of the pure and composite PQDs are compared in Figure 9 and were calculated using $\sigma_{ph} = \frac{\alpha nc}{4\pi}$ [43]. The composite had a higher optical conductivity at all photon excitation energies, except for a small difference above 3.00 eV in the UV region. The improved optical conductivity shows that EVA-TPR/PQD films can increase the mobility of excitons and free charge carriers. The potential gradient at the surface interface between the PQDs and the EVA-TPR could enhance charge separation (splitting

of electrons and holes from tightly bound excitons). However, increasing the quantity of EVA-TPR or any polymer matrix may not always improve the optical performance because the EVA-TPR material has an inherently low conductivity.

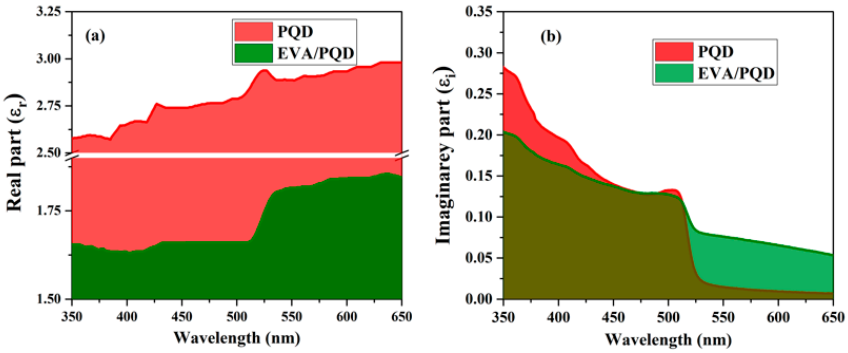

Figure 8. (**a**) Real and (**b**) imaginary parts of the complex dielectric constant of the pure PQD and the EVA-TPR/PQD films.

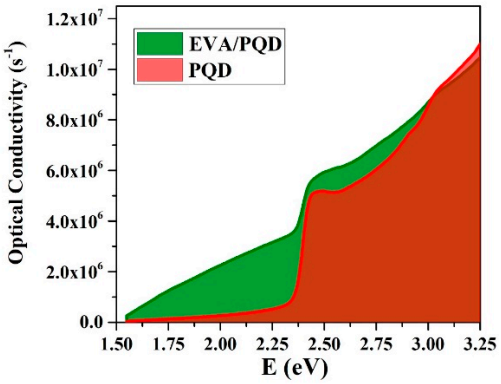

Figure 9. Optical conductivity of the pure PQD and the EVA-TPR/PQD films.

The optical stability of the pure PQD and the EVA-TPR/PQD films was measured by exposing the films to nanosecond pulses (355 nm, 2 mJ, 10 ns pulse width). The EVA-TPR/PQD withstood more than 1000 pulses without significant loss in the output fluorescence, but pure PQD started degrading after 200 pulses, and output fluorescence dropped to 10%.

4. Conclusions

In this study, we compared the optical performances of thin films made of pure $CsPbBr_3$ and EVA-TPR/(PQDs-$CsPbBr_3$). The optical performances of the pure $CsPbBr_3$ and the EVA-TPR/PQDs were experimentally determined by measuring the photoluminescence, absorption, transmission, and reflectance. The PL intensity of the EVA-TPR/PQDs was twice that of the PQDs. The absorbance spectrum of the EVA-TPR/PQDs exhibited a primary shoulder band at 507 nm with a long tail because of the amorphous nature of the EVA-TPR polymer. Calculations showed that the direct band gap of the EVA-TPR/PQDs (2.202 eV) was lower than that of the pure PQDs (2.304 eV). Similarly, the indirect band gap was 2.33 eV for the composite and 2.38 eV for the pure PQDs. The transition slope occurred at almost the same place for the direct and indirect band gaps, indicating an efficient radiative transition. The addition of EVA did not deteriorate the performance of the PQDs but, rather, improved it. This study was extended to the analysis of the absorption and extinction coefficients and confirmed the improved performance of the EVA/PQDs. Next, we investigated the refractive index and the dielectric constant (real and imaginary), which showed that the EVA/PQD composites are suitable for solar cells and other photonic devices. Finally, the optical conductivity of the films was studied.

All the above analyses showed that the EVA/PQDs were more efficient and stable both physically and optically. Hence, the EVA/PQDs could be suitable copolymer/perovskite active materials for optoelectronic devices, such as solar cells and perovskite/polymer light-emitting diodes (PPLEDs).

Author Contributions: Conceptualization, M.S.A., M.J.A., and S.P.; methodology, M.J.A.; software, M.J.A. and S.P.; validation, S.P., M.S.A. and M.J.A.; formal analysis, S.P.; investigation, M.J.A. and A.A.; resources, M.S.A.; data curation, S.P. and M.J.A.; writing—original draft preparation, S.P. and M.J.A.; writing—review and editing, M.S.A.; visualization, S.P. and M.J.A.; supervision, M.S.A.; project administration M.S.A. All authors have read and agreed to the published version of the manuscript.

Institutional Review Board Statement: Not applicable.

Informed Consent Statement: Not applicable.

Data Availability Statement: The data is available with corresponding author for reasonable request.

Acknowledgments: This project was funded by the National Plan for Science, Technology, and Innovation (MAARIFAH), King Abdulaziz City for Science and Technology, Kingdom of Saudi Arabia, award number (14-ENE899-02).

Conflicts of Interest: The authors declare no conflict of interest.

References

1. Kim, H.-S.; Lee, C.-R.; Im, J.-H.; Lee, K.-B.; Moehl, T.; Marchioro, A.; Moon, S.-J.; Humphry-Baker, R.; Yum, J.-H.; Moser, J.E. Lead iodide perovskite sensitized all-solid-state submicron thin film mesoscopic solar cell with efficiency exceeding 9%. *Sci. Rep.* **2012**, *2*, 1–7. [CrossRef]
2. Kojima, A.; Teshima, K.; Shirai, Y.; Miyasaka, T. Organometal halide perovskites as visible-light sensitizers for photovoltaic cells. *J. Am. Chem. Soc.* **2009**, *131*, 6050–6051. [CrossRef]
3. Kumawat, N.K.; Gupta, D.; Kabra, D. Recent Advances in Metal Halide-Based Perovskite Light-Emitting Diodes. *Energy Technol.* **2017**, *5*, 1734–1749. [CrossRef]
4. Chen, Y.; Chu, Y.; Wu, X.; Ou-Yang, W.; Huang, J. High-Performance Inorganic Perovskite Quantum Dot–Organic Semiconductor Hybrid Phototransistors. *Adv. Mater.* **2017**, *29*, 1–8. [CrossRef] [PubMed]
5. Eperon, G.E.; Paternò, G.M.; Sutton, R.J.; Zampetti, A.; Haghighirad, A.A.; Cacialli, F.; Snaith, H.J. Inorganic caesium lead iodide perovskite solar cells. *J. Mater. Chem. A* **2015**, *3*, 19688–19695. [CrossRef]
6. Kim, Y.C.; Kim, K.H.; Son, D.-Y.; Jeong, D.-N.; Seo, J.-Y.; Choi, Y.S.; Han, I.T.; Lee, S.Y.; Park, N.-G. Printable organometallic perovskite enables large-area, low-dose X-ray imaging. *Nature* **2017**, *550*, 87–91. [CrossRef]
7. Huang, C.Y.; Zou, C.; Mao, C.; Corp, K.L.; Yao, Y.C.; Lee, Y.J.; Schlenker, C.W.; Jen, A.K.Y.; Lin, L.Y. $CsPbBr_3$ Perovskite Quantum Dot Vertical Cavity Lasers with Low Threshold and High Stability. *ACS Photonics* **2017**, *4*, 2281–2289. [CrossRef]
8. Yassitepe, E.; Yang, Z.; Voznyy, O.; Kim, Y.; Walters, G.; Castañeda, J.A.; Kanjanaboos, P.; Yuan, M.; Gong, X.; Fan, F. Amine-free synthesis of cesium lead halide perovskite quantum dots for efficient light-emitting diodes. *Adv. Funct. Mater.* **2016**, *26*, 8757–8763. [CrossRef]
9. Sun, C.; Zhang, Y.; Ruan, C.; Yin, C.; Wang, X.; Wang, Y.; Yu, W.W. Efficient and stable white LEDs with silica-coated inorganic perovskite quantum dots. *Adv. Mater.* **2016**, *28*, 10088–10094. [CrossRef]
10. Song, J.; Li, J.; Li, X.; Xu, L.; Dong, Y.; Zeng, H. Quantum Dot Light-Emitting Diodes Based on Inorganic Perovskite Cesium Lead Halides ($CsPbX_3$). *Adv. Mater.* **2015**, *27*, 7162–7167. [CrossRef]
11. Deschler, F.; Price, M.; Pathak, S.; Klintberg, L.E.; Jarausch, D.-D.; Higler, R.; Hüttner, S.; Leijtens, T.; Stranks, S.D.; Snaith, H.J. High photoluminescence efficiency and optically pumped lasing in solution-processed mixed halide perovskite semiconductors. *J. Phys. Chem. Lett.* **2014**, *5*, 1421–1426. [CrossRef]
12. Gholipour, S.; Saliba, M. Bandgap tuning and compositional exchange for lead halide perovskite materials. In *Characterization Techniques for Perovskite Solar Cell Materials*; Elsevier: Amsterdam, The Netherlands, 2020; pp. 1–22.
13. Han, T.-H.; Lee, J.-W.; Choi, C.; Tan, S.; Lee, C.; Zhao, Y.; Dai, Z.; De Marco, N.; Lee, S.-J.; Bae, S.-H. Perovskite-polymer composite cross-linker approach for highly-stable and efficient perovskite solar cells. *Nat. Commun.* **2019**, *10*, 1–10. [CrossRef] [PubMed]
14. Peng, L.; Tang, A.; Yang, C.; Teng, F. Size-controlled synthesis of highly luminescent organometal halide perovskite quantum dots. *J. Alloys Compd.* **2016**, *687*, 506–513. [CrossRef]
15. Yang, G.-L.; Zhong, H.-Z. Organometal halide perovskite quantum dots: Synthesis, optical properties, and display applications. *Chin. Chem. Lett.* **2016**, *27*, 1124–1130. [CrossRef]
16. Protesescu, L.; Yakunin, S.; Bodnarchuk, M.I.; Krieg, F.; Caputo, R.; Hendon, C.H.; Yang, R.X.; Walsh, A.; Kovalenko, M.V. Nanocrystals of Cesium Lead Halide Perovskites ($CsPbX_3$, X = Cl, Br, and I): Novel Optoelectronic Materials Showing Bright Emission with Wide Color Gamut. *Nano Lett.* **2015**, *15*, 3692–3696. [CrossRef]

17. Levchuk, I.; Osvet, A.; Tang, X.; Brandl, M.; Perea, J.D.; Hoegl, F.; Matt, G.J.; Hock, R.; Batentschuk, M.; Brabec, C.J. Brightly luminescent and color-tunable formamidinium lead halide perovskite $FAPbX_3$ (X= Cl, Br, I) colloidal nanocrystals. *Nano Lett.* **2017**, *17*, 2765–2770. [CrossRef]
18. Liu, Z.; Zhang, Y.; Fan, Y.; Chen, Z.; Tang, Z.; Zhao, J.; Lv, Y.; Lin, J.; Guo, X.; Zhang, J. Toward highly luminescent and stabilized silica-coated perovskite quantum dots through simply mixing and stirring under room temperature in air. *ACS Appl. Mater. Interfaces* **2018**, *10*, 13053–13061. [CrossRef]
19. Meyns, M.; Perálvarez, M.; Heuer-Jungemann, A.; Hertog, W.; Ibáñez, M.; Nafria, R.; Genç, A.; Arbiol, J.; Kovalenko, M.V.; Carreras, J. Polymer-enhanced stability of inorganic perovskite nanocrystals and their application in color conversion LEDs. *ACS Appl. Mater. Interfaces* **2016**, *8*, 19579–19586. [CrossRef]
20. Li, Z.; Hofman, E.; Li, J.; Davis, A.H.; Tung, C.; Wu, L.; Zheng, W. Photoelectrochemically active and environmentally stable $CsPbBr_3/TiO_2$ core/shell nanocrystals. *Adv. Funct. Mater.* **2018**, *28*, 1704288. [CrossRef]
21. Aljaafreh, M.J.; Prasad, S.; AlSalhi, M.S.; Lemmer, U.; Alahmed, Z.A.; Baloch, M.A. Emission dynamics of conjugated oligomer (BECV-DHF)/quantum dot perovskite ($CsPbBr_3$) composites in solutions. *Colloids Surf. A Physicochem. Eng. Asp.* **2021**, *610*, 125911. [CrossRef]
22. Yang, H.; Yin, W.; Dong, W.; Gao, L.; Tan, C.-H.; Li, W.; Zhang, X.; Zhang, J. Enhancing the light-emitting performance and stability in $CsPbBr_3$ perovskite quantum dots via simultaneous doping and surface passivation. *J. Mater. Chem. C* **2020**, *8*, 14439–14445. [CrossRef]
23. Xiang, Q.; Zhou, B.; Cao, K.; Wen, Y.; Li, Y.; Wang, Z.; Jiang, C.; Shan, B.; Chen, R. Bottom up stabilization of $CsPbBr_3$ quantum dots-silica sphere with selective surface passivation via atomic layer deposition. *Chem. Mater.* **2018**, *30*, 8486–8494. [CrossRef]
24. Wu, Y.; Wei, C.; Li, X.; Li, Y.; Qiu, S.; Shen, W.; Cai, B.; Sun, Z.; Yang, D.; Deng, Z. In situ passivation of PbBr64–octahedra toward blue luminescent $CsPbBr_3$ nanoplatelets with near 100% absolute quantum yield. *ACS Energy Lett.* **2018**, *3*, 2030–2037. [CrossRef]
25. Wang, H.; Lin, S.; Tang, A.; Singh, B.P.; Tong, H.; Chen, C.; Lee, Y.; Tsai, T.; Liu, R. Mesoporous silica particles integrated with all-inorganic $CsPbBr_3$ perovskite quantum-dot nanocomposites (MP-PQDs) with high stability and wide color gamut used for backlight display. *Angew. Chem. Int. Ed.* **2016**, *55*, 7924–7929. [CrossRef]
26. Li, Z.; Kong, L.; Huang, S.; Li, L. Highly luminescent and ultrastable $CsPbBr_3$ perovskite quantum dots incorporated into a silica/alumina monolith. *Angew. Chem.* **2017**, *129*, 8246–8250. [CrossRef]
27. Shen, X.; Sun, C.; Bai, X.; Zhang, X.; Wang, Y.; Wang, Y.; Song, H.; Yu, W.W. Efficient and stable $CsPb(Br/I)_3$@ anthracene composites for white light-emitting devices. *ACS Appl. Mater. Interfaces* **2018**, *10*, 16768–16775. [CrossRef]
28. He, Z.; He, J.; Zhang, C.; Wu, S.; Dong, Y. Swelling-Deswelling Microencapsulation-Enabled Ultrastable Perovskite− Polymer Composites for Photonic Applications. *Chem. Rec.* **2020**, *20*, 672–681. [CrossRef]
29. Chen, L.-C.; Tien, C.-H.; Tseng, Z.-L.; Dong, Y.-S.; Yang, S. Influence of PMMA on all-inorganic halide perovskite $CsPbBr_3$ quantum dots combined with polymer matrix. *Materials* **2019**, *12*, 985. [CrossRef]
30. Carrillo-Carrión, C.; del Pino, P.; Pelaz, B. Aqueous stable luminescent perovskite-polymer composites. *Appl. Mater. Today* **2019**, *15*, 562–569. [CrossRef]
31. Li, Y.; Lv, Y.; Guo, Z.; Dong, L.; Zheng, J.; Chai, C.; Chen, N.; Lu, Y.; Chen, C. One-step preparation of long-term stable and flexible $CsPbBr_3$ perovskite quantum dots/ethylene vinyl acetate copolymer composite films for white light-emitting diodes. *ACS Appl. Mater. Interfaces* **2018**, *10*, 15888–15894. [CrossRef]
32. Gao, Y.; Guo, N.; Gauvreau, B.; Rajabian, M.; Skorobogata, O.; Pone, E.; Zabeida, O.; Martinu, L.; Dubois, C.; Skorobogatiy, M. Consecutive solvent evaporation and co-rolling techniques for polymer multilayer hollow fiber preform fabrication. *J. Mater. Res.* **2006**, *21*, 2246–2254. [CrossRef]
33. Skorobogatiy, M. Efficient antiguiding of TE and TM polarizations in low-index core waveguides without the need for an omnidirectional reflector. *Opt. Lett.* **2005**, *30*, 2991. [CrossRef]
34. Becker, H.; Locascio, L.E. Polymer microfluidic devices. *Talanta* **2002**, *56*, 267–287. [CrossRef]
35. Ilican, S.; Caglar, M.; Caglar, Y. Determination of the thickness and optical constants of transparent indium-doped ZnO thin films by the envelope method. *Mater. Sci. Pol.* **2007**, *25*, 709–718.
36. Dahshan, A.; Aly, K.A. Determination of the thickness and optical constants of amorphous Ge-Se-Bi thin films. *Philos. Mag.* **2009**, *89*, 1005–1016. [CrossRef]
37. Ghosh, S.; Lima, A.H.; Flôres, L.S.; Pacheco, T.S.; Barbosa, A.A.; Ullah, S.; de Mendonça, J.P.A.; Oliveira, L.F.C.; Quirino, W.G. Growth and characterization of ammonium nickel-copper sulfate hexahydrate: A new crystal of Tutton's salt family for the application in solar-blind technology. *Opt. Mater.* **2018**, *85*, 425–437. [CrossRef]
38. Gong, J.; Krishnan, S. Chapter 2—Mathematical Modeling of Dye-Sensitized Solar Cells. In *Dye-Sensitized Solar Cells: Mathematical Modeling, and Materials Design and Optimization*; Soroush, M., Lau, K.K.S., Eds.; Academic Press: Cambridge, MA, USA, 2019; pp. 51–81. ISBN 978-0-12-814541-8.
39. Mayerhöfer, T. The Bouguer-Beer-Lambert Law: Shining Light on the Obscure the Bouguer-Beer-Lambert Law: Shining Light on the Obscure. *ChemPhysChem* **2020**, *21*, 2029. [CrossRef]
40. Rahman, M.F.; Hossain, J.; Ismail, A.B.M. Structural, surface morphological and optical properties and their correlation with the thickness of spin coated superior quality CdS thin film synthesized using a novel chemical route. *SN Appl. Sci.* **2020**, *2*, 2–10. [CrossRef]

41. Yin, W.J.; Shi, T.; Yan, Y. Unique properties of halide perovskites as possible origins of the superior solar cell performance. *Adv. Mater.* **2014**, *26*, 4653–4658. [CrossRef] [PubMed]
42. Roknuzzaman, M.; Zhang, C.; Ostrikov, K.K.; Du, A.; Wang, H.; Wang, L.; Tesfamichael, T. Electronic and optical properties of lead-free hybrid double perovskites for photovoltaic and optoelectronic applications. *Sci. Rep.* **2019**, *9*, 1–7. [CrossRef]
43. Shankar, J.S.; Ashok Kumar, S.; Periyasamy, B.K.; Nayak, S.K. Studies on Optical Characteristics of Multicolor Emitting MEH-PPV/ZnO Hybrid Nanocomposite. *Polym. Technol. Mater.* **2019**, *58*, 148–157. [CrossRef]
44. Arslan, M.; Duymuş, H.; Yakuphanoglu, F. Optical Properties of the Poly(N-benzylaniline) Thin Film. *J. Phys. Chem. B* **2006**, *110*, 276–280. [CrossRef]